RSC Advances

ROYAL SOCIETY OF CHEMISTRY

www.rsc.org/advances

Korea Advanced Institute of Science and Technology
291 Daehak-ro, Yuseong-gu Daejeon 305-701 Korea | Tel: +82-42-350-3329 | Email: idkim@kaist.ac.kr

Dec. 8, 2014

Graphical Abstract (ToC)

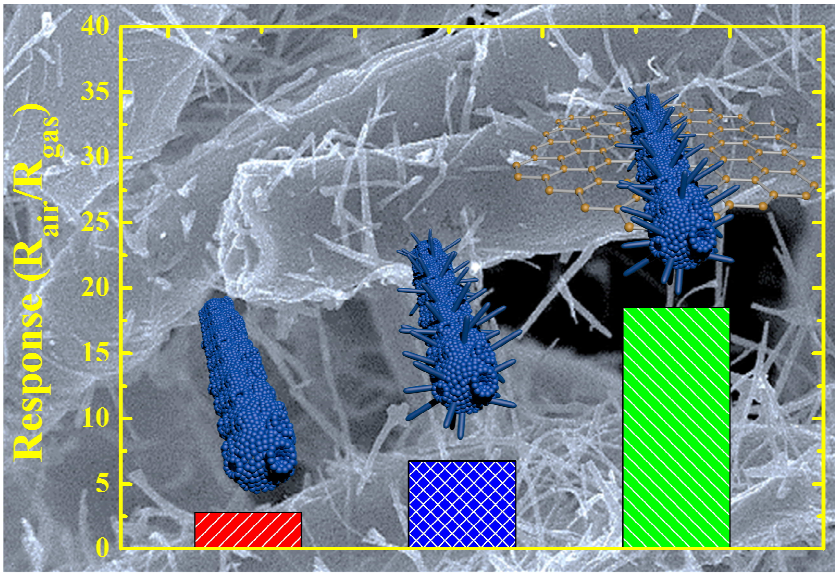

Hierarchical and porous structure of one-dimensional (1D) nonwoven WO_3 nanofibers having randomly oriented 1D nanoneedles as well as multiple pores on the surface were synthesized by electrospinning and controlled two-step heat-treatment, which is applicable for diabetes diagnostic sensors by selective detection of breath acetone.

RSC Advances

RSCPublishing

COMMUNICATION

Facile synthesis of hierarchical porous WO_3 nanofibers having 1D nanoneedles and their functionalization with non-oxidized graphene flakes for selective detection of acetone molecules

Cite this: DOI: 10.1039/x0xx00000x

Received 00th January 2012,
Accepted 00th January 2012

DOI: 10.1039/x0xx00000x

www.rsc.org/

Seon-Jin Choi,[a] Chanyong Choi,[b] Sang-Joon Kim,[a] Hee-Jin Cho,[a] Seokwoo Jeon[b] and Il-Doo Kim*[a]

Multiple pore-loaded (1D) WO_3 nanofibers (NFs) having 1D nanoneedle branches were successfully synthesized by polystyrene-colloid-template-assisted electrospinning followed by a two-step heat-treatment. Randomly branched WO_3 nanoneedles and high porosity effectively facilitated the surface reaction with acetone molecules. In addition, the hierarchical porous WO_3 NFs were further functionalized with catalytic non-oxidized graphene (NOGR) flakes, which showed dramatically improved acetone sensing performance. The result demonstrated the high potential for application in the diagnosis of diabetes by breath acetone analysis.

Human exhaled breath analysis is getting a great deal of attention since it is a non-invasive and simple diagnostic method. A number of diseases, such as lung cancer,[1] asthma,[2] and halitosis,[3] can be diagnosed in breath by detection of biomarkers such as toluene ($C_6H_5CH_3$), nitrogen monoxide (NO), and hydrogen sulfide (H_2S). Moreover, diabetes patients can be diagnosed by measuring breath acetone (CH_3COCH_3) concentration.[4] The acetone concentration of a diabetes patient contains over 1.8 ppm, which is 2–6 times higher than that of a healthy human (300–900 ppb).[5] Thus far, several types of exhaled breath sensors have been proposed and have demonstrated non-invasive diagnosis of diseases by sensitive and selective detection of biomarkers. Generally, highly sensitive equipment such as gas chromatography and mass spectroscopy (GC-MS) is used for the analysis of exhaled breath components.[6] However, GC-MS has critical disadvantages such as bulky size, high cost, and complexity of manipulation, which limits the practical application for real-time monitoring and portable devices.

Recently, semiconductor metal oxides (SMOs) have received a great deal of attention for exhaled breath sensors considering the low cost for material preparation and high potential for portable sensor by miniaturization.[7] In addition, the simple measurement principle, i.e., resistivity changes when exposed to a specific gas ambient, derives practical application for wide use.[8] Maximization of the specific surface area and porosity of SMO is the foremost criteria to achieve high sensitivity because the gas reaction mainly occurs on the surface of SMO. For this reason, nanostructured SMOs such as one-dimensional (1D) SnO_2 nanofibers,[9] ZnO nanowires,[10] WO_3 columnar structure,[11] and Zn-Ti-O-based nanofibers,[12] as well as three-dimensional (3D) spherical nanostructures of SnO_2 spheres[13-15] and WO_3 spheres[16] were proposed to detect specific gas molecules. To further improve the sensing characteristics, hierarchical structures are desired considering the increased surface reaction sites.[17] The hierarchical structures of α-Fe_2O_3/NiO,[18] ZnO,[19] and CuO[20] are examples of candidates for application in highly sensitive gas sensing layers. However, the synthetic method of hierarchical structures often involves complicated chemical solution processes as well as the addition of chemical additives, which complicates the synthesis of hierarchical SMO nanostructures. As a facile synthetic technique for 1D nanowires, heat-treatment in certain ambient was proposed and produced well-defined nanowires such as CuO,[21] ZnO,[22] and MgO.[23] However, heat-treatment-assisted nanowire

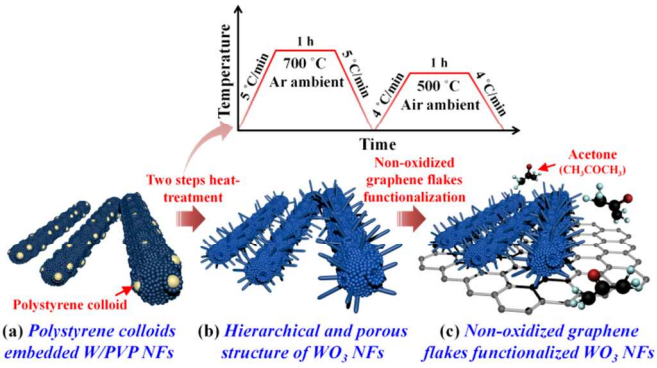

Scheme 1 (a) Polystyrene colloids embedded as-spun W precursor/PVP composite nanofibers (NFs), (b) hierarchical and porous WO_3 (H-WO_3) NFs synthesized by controlled heat-treatment at 700 ˚C in Ar ambient followed by subsequent oxidation at 500 ˚C for in air ambient, and (c) non-oxidized graphene flake functionalized H-WO_3 NFs.

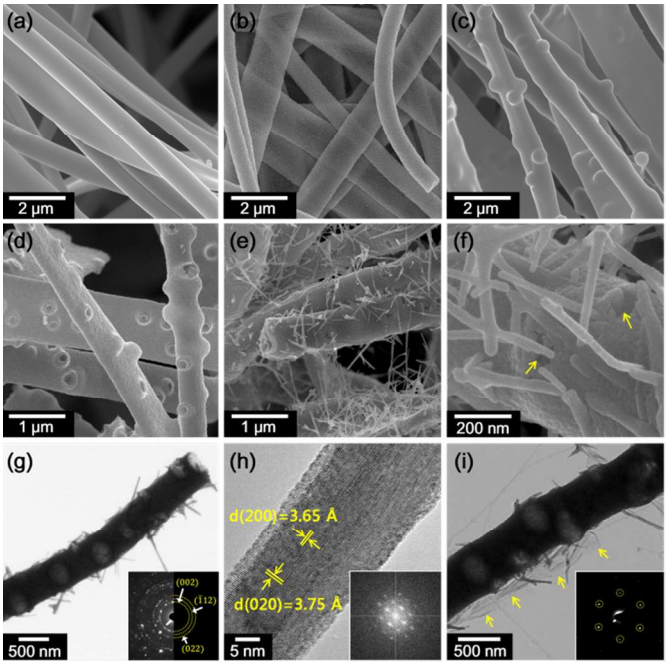

Fig. 1 Morphologies and crystal structures of synthesized WO_3 nanofibers (NFs) functionalized by non-oxidized graphene (NOGR) flakes: SEM image of (a) as-spun W precursor/PVP composite NFs, (b) dense WO_3 NFs after calcination at 500 ˚C for 1 h in air, (c) as-spun W precursor/PVP composite NFs containing polystyrene (PS) colloid templates, (d) porous WO_3 NFs synthesized by the PS colloid templating route after calcination at 500 ˚C for 1 h in air, (e) hierarchical and porous WO_3 (H-WO_3) NFs synthesized by reduction at 700 ˚C for 1 h in Ar ambient followed by subsequent oxidation at 500 ˚C for 1 h in air, (f) magnified SEM image of (e), (g) TEM image of H-WO_3 NF with the selected area electron diffraction (SAED) pattern in the inset, (h) high-resolution TEM image of a nanoneedle on the surface of an H-WO_3 NF with the FFT pattern in the inset, and (i) TEM image of H-WO_3 NF functionalized by NOGR flakes (yellow arrows) with the SAED pattern of NOGR flakes in the inset.

growth was mainly performed on the flat surface, i.e. film or foil, and the growth on the nanofibrous non-woven structure has never been demonstrated.

In addition to the structural modification of SMOs, catalytic nanoparticles, such as Pt, Pd, Au, and Ag, were functionalized to the nanostructured SMO surface to promote a surface reaction, thereby improving sensitivity as well as selectivity.[24] More recently, graphene-based catalytic materials were functionalized with SMOs to induce a catalytic effect.[25-27] However, functionalization of non-oxidized graphene flakes as catalytic material has rarely been attempted or demonstrated.

In this work, we propose a facile and versatile synthetic method for the hierarchical and porous structure of WO_3 nanofibers (hereafter, H-WO_3 NFs) functionalized with non-oxidized graphene (NOGR) flakes for highly sensitive and selective exhaled acetone sensing layers for potential diagnosis of diabetes. The H-WO_3 NFs were prepared by electrospinning of W precursor (ammonium metatungstate hydrate) /Polyvinylpyrrolidone (PVP) *via* the polystyrene (PS) templating route (Scheme 1a) followed by a two-steps heat-treatment in reducing Ar and oxidizing air ambient (Scheme 1b) (see ESI†). As a result, a hierarchical and porous WO_3 NF structure having multiple pores as well as 1D nanoneedles on the surface of WO_3 NFs was obtained. In addition, highly conductive NOGR flakes exfoliated from a graphite intercalation compound (GIC) were functionalized with the H-WO_3 NFs to enhance the sensing performance (Scheme 1c).

Fig. 1 shows the microstructural and morphological observation of H-WO_3 NFs. The electrospun W precursor/PVP composite NFs exhibited non-woven structure having an average diameter of 800 nm with smooth surface morphology (Fig. 1a). Then, calcination was performed at 500 ˚C in air for 1 h to decompose PVP and oxidize the W precursor. The synthesized WO_3 NFs exhibited similar non-woven structure, exhibiting a shrunk average diameter of 700 nm as compared to the W precursor/PVP composite NFs (Fig. 1b). However, dense structure composed of aggregated WO_3 grains was obtained (see ESI†, Fig. S1). To achieve porous WO_3 NFs, insoluble PS colloids with a diameter of 500 nm were introduced in the electrospinning solution as sacrificial templates (See ESI†). The PS colloids embedded as-spun W precursor/PVP (hereafter, W precursor/PVP/PS) composite NFs exhibited rugged surface morphology, which was attributed to the spherical PS colloid templates (Fig. 1c). Then, high-temperature calcination was performed at 500 ˚C for 1 h in air, which resulted in porous WO_3 (PS-WO_3) NFs due to the decomposition of the PS colloid template (Fig. 1d). Multiple pores were observed on the surface as well as inside of the PS-WO_3 NFs (see ESI†, Fig. S1). To achieve H-WO_3 NFs, the heat-treatment process was controlled with two steps in which the as-spun W precursor/PVP/PS composite NFs were calcined at 700 ˚C for 1 h in Ar ambient followed by oxidation at 500 ˚C for 1 h in air atmosphere. The obtained H-WO_3 NFs exhibited branched nanoneedles on the surface of WO_3 NFs (Fig. 1e). Moreover, large pores (yellow arrows) formed by the decomposition of PS colloid templates were observed on the surface of the WO_3 NFs (Fig. 1f). TEM analysis was performed with H-WO_3 NFs to confirm the detailed morphological and crystal structure (Figs. 1g-i). As shown in Fig. 1g, open pores on the surface as well as closed pores in the WO_3 NFs were clearly observed with the randomly-oriented nanoneedles. In addition, polycrystalline structures of H-WO_3 NFs were identified by a selected area electron diffraction (SAED) pattern exhibiting the crystal plans of (002), ($\bar{1}$12), and (022) (Fig. 1g in the inset). High-resolution TEM images and fast Fourier transform (FFT) patterns revealed that a highly crystalized WO_3 nanoneedle was identified with interplanar distances of 3.65 Å and 3.75 Å, which correspond to the crystal planes of (200) and (020), respectively, as shown in Fig. 1h. Through energy-dispersive X-ray spectroscopy (EDS) elemental mapping analysis, it was found that the nanoneedles were composed of W and O (see ESI†, Fig. S2). X-ray diffraction (XRD) analysis revealed that highly crystalized structures of dense WO_3 NFs and H-WO_3 NFs having monoclinic phase were identified (see ESI†, Fig. S3).

To understand the mechanism of nanoneedle growth on the surface of WO_3 NFs, we performed SEM and TEM observation with the sample of as-spun W precursor/PVP/PS composite NFs after heat-treatment at 700 ˚C in Ar ambient, which conformed the formation of WO_3 nanoneedles (see ESI†, Fig. S4). Typically, an oxygen-deficient form of tungsten oxide, e.g., $W_{18}O_{49}$, can be formed after heat-treatment in Ar ambient.[28] However, we found that the nanoneedles had a WO_3 phase, which was ascribed to the use of the W precursor, i.e., $(NH_4)_6H_2W_{12}O_{40}\cdot xH_2O$, containing sufficient oxygen. The growth mechanism of WO_3 phase nanoneedles can be explained by a vapor-solid growth process because the growth

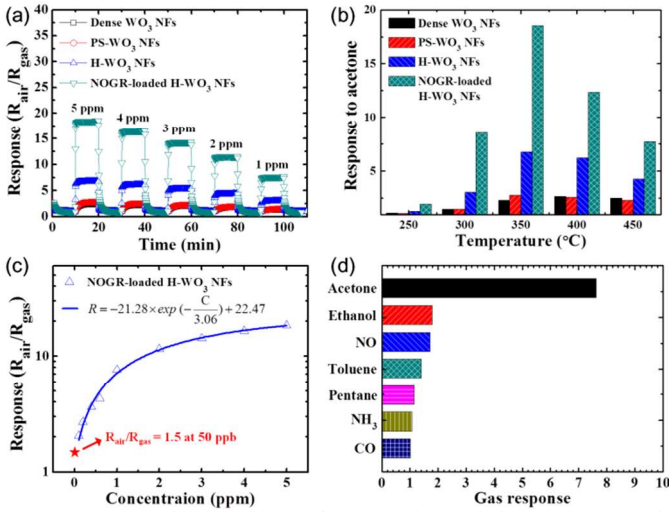

Fig. 2 (a) Dynamic response (R_{air}/R_{gas}) transition of the sensors toward acetone at 350 ˚C in a concentration range of 1–5 ppm, (b) temperature-dependent response characteristics toward acetone at 5 ppm in the temperature range of 250–450 ˚C, (c) limit of detection characteristic and (d) selective detection characteristic of NOGR-loaded H-WO_3 NFs toward acetone and interfering analytes at 1 ppm.

occurred without a metallic catalyst. In addition, solid phase diffusion of W atoms in the preference direction, i.e., [010], from the W precursor/PVP/PS composite NFs, occurred by forming WO_3 nanoneedles on the surface, which resulted in the hierarchical structure of WO_3 NFs after subsequent oxidation. This observation of nanoneedle formation was in good agreement with previous reports.[29, 30] The diameter and length distributions were investigated, and it was found that WO_3 nanoneedles after heat-treatment in reducing Ar ambient at 700 ˚C showed the diameter and length in the ranges of 8–20 nm and 130–700 nm, respectively, whereas the diameter and length distributions were changed to 15–40 nm and 200 nm–1 μm, respectively, after subsequent heat-treatment in air ambient at 500 ˚C. The diameter and the length of the WO_3 nanoneedles can be further optimized by controlling the heat-treatment temperature and time.[21]

The synthesized H-WO_3 NFs were dispersed in ethanol and functionalized with highly conductive NOGR flakes to further increase the sensing performance by the catalytic sensitization effect. A very thin layer of NOGR flakes, which were prepared by exfoliation from a GIC and dispersed in acetone solution, were attached to the H-WO_3 NFs by mixing each dispersed solution as shown in Fig. 1i (yellow arrows) (See ESI†).[31-33] The characteristic SAED pattern of NOGR flakes showed the hexagonal pattern of a crystallite graphene structure (Fig. 1i in the inset).[34]

Gas sensing characteristics were investigated in a highly humid atmosphere (90% RH) to demonstrate their potential use in exhaled breath analysis for the diagnosis of diabetes (Fig. 2). Fig. 2a shows the dynamic response (R_{air}/R_{gas}) transition characteristic of dense WO_3 NFs, PS-WO_3 NFs, H-WO_3 NFs, and NOGR-loaded H-WO_3 NFs toward acetone in a concentration range of 1–5 ppm at 350 ˚C. The result revealed that the response (R_{air}/R_{gas} = 6.8) of H-WO_3 NFs exhibited almost a 3-fold increase compared to that (R_{air}/R_{gas} = 2.3) of dense WO_3 NFs. Moreover, the response (R_{air}/R_{gas} = 18.5) of NOGR-loaded WO_3 NFs showed over an 8-fold and 2.7-fold increase compared to that of dense WO_3 NFs (R_{air}/R_{gas} = 2.3) and H-WO_3 NFs (R_{air}/R_{gas} = 6.8), respectively. The optimum acetone

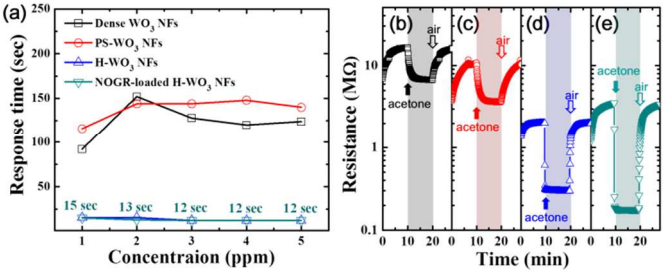

Fig. 3 (a) Response time characteristics of dense WO_3 NFs, PS-WO_3 NFs, H-WO_3 NFs, and NOGR-loaded H-WO_3 NFs toward acetone in a concentration range of 1–5 ppm at 350 ˚C. Dynamic resistance changes of (b) dense WO_3 NFs, (c) PS-WO_3 NFs, (d) H-WO_3 NFs, and (e) NOGR-loaded H-WO_3 NFs at 5 ppm of acetone and operating temperature at 350 ˚C.

response characteristic with respect to the operating temperature was investigated in the temperature range of 250–450 ˚C, where all sensors exhibited highest response at 350 ˚C (Fig. 2b). For the limit of detection capability, the NOGR-loaded H-WO_3 NFs was capable of detection of 100 ppb of acetone exhibiting a response (R_{air}/R_{gas}) of 2 (see ESI†, Fig. S5). In addition, exponential approximation identified that 50 ppb of acetone can be measured with a response of 1.5 (Fig. 2c). The detection selectivity of NOGR-loaded H-WO_3 NFs was high enough with a high response of 7.6 toward 1 ppm acetone at 350 ˚C with minor response (R_{air}/R_{gas} < 1.8) toward interfering gases such as ethanol (C_2H_5OH), nitrogen monoxide (NO), toluene ($C_6H_5CH_3$), pentane (C_5H_{12}), ammonia (NH_3), and carbon monoxide (CO), which are known as exhaled breath components. For application in real-time diagnosis, fast response time is an essential parameter for exhaled breath sensors. Therefore, the response times of dense WO_3 NFs, PS-WO_3 NFs, H-WO_3 NFs, and NOGR-loaded H-WO_3 NFs were confirmed by measuring the average elapsed time to reach 90% saturation in response to an acetone concentration range of 1–5 ppm (Fig. 3a). Very short average response times (12.8 sec) of H-WO_3 NFs and NOGR-loaded H-WO_3 NFs were observed compared to those of PS-WO_3 NFs (138.4 sec) and dense WO_3 NFs (123.2 sec). The fast response time was also evidently confirmed by resistivity changes of sensors when 5 ppm of acetone was exposed at an operating temperature of 350 ˚C (Figs. 3b-e). The fast responding speeds as well as high response (large resistance change) of H-WO_3 NFs and NOGR-loaded H-WO_3 NFs demonstrated the potential application for real-time breath analysis.

The dramatically improved sensing characteristics with H-WO_3 NFs and NOGR-loaded H-WO_3 NFs were investigated. The dominant factor of the enhanced sensing property was the increased surface reaction sites and porosity of the H-WO_3 NFs, which was attributed to the formation of WO_3 nanoneedles and open pores on the surface of WO_3 NFs. Effective modulation of surface depletion layers formed by chemisorbed oxygen species (O^{2-}, O^-, and O_2^-) can be achieved on the H-WO_3 NFs surface due to the increased surface area. The adsorbed oxygen species attract electrons from the conduction band of the WO_3 NFs by thickening the depletion layers. When the reducing analytes such as acetone are exposed, the adsorbed oxygen species will be eliminated on the surface while donating electrons back to the conduction band of the WO_3 NFs according to the following reaction: CH_3COCH_3 (gas) + O^- → $CH_3COC^+H_2$ + OH^- + e^- or CH_3COCH_3 (gas) + $2O^-$ → C^+H_3 + CO_2 + CH_3O^- + $2e^-$.[35] This results in high resistivity changes by thinning

the depletion layers. For the NOGR-loaded WO_3 NFs, highly conductive NOGR flakes enable catalytic (electronic) sensitization integrated with H-WO_3 NFs by exchanging electrons during gas exposure. In other words, the higher work function of NOGR flakes (Φ=4.67 eV) (see ESI†, Fig. S6a) compared to that of WO_3 NFs (Φ=4.56 eV) (see ESI†, Fig. S6b) drives effective electron transfer from WO_3 NFs to NOGR flakes by forming a Schottky barrier of 0.11 eV, which resulted in large conductivity changes by modulating the electron concentration in WO_3 NFs when a target analyte was injected.

Conclusions

In summary, a facile and versatile synthetic method of hierarchical 1D-1D nanostructures, i.e., 1D WO_3 nanoneedles formed on the surface of porous 1D WO_3 NFs, were achieved by two-step annealing, i.e., an initial heat-treatment in reduced atmosphere prior to the second calcination step in air. It is a great advantage to synthesize 1D WO_3 nanoneedles on the fibrous nonwoven WO_3 nanostructure by simply controlling the heat-treatment in Ar ambient. The synthesized 1D WO_3 NFs exhibited a diameter of 700 nm with randomly oriented 1D nanoneedles having average diameters of 15–40 nm and lengths of 200 nm–1 μm, which showed large size distribution in diameters of 1D WO_3 nanostructures. The unique morphology and structure generated enhanced acetone sensing performance at highly humid ambient (90% RH), which was attributed to the increased surface reaction sites. In addition, effective catalytic sensitization of NOGR flakes in the composite of NOGR-loaded H-WO_3 NFs resulted in the dramatically improved acetone sensing performance. The NOGR-loaded H-WO_3 NFs exhibited superior sensitivity (R_{air}/R_{gas} = 18.5 at 5 ppm), which was an 8-fold improved response compared to that of dense WO_3 NFs toward acetone and remarkable selectivity with minor responses (R_{air}/R_{gas} < 1.8) toward interfering analytes. In addition, very fast responding speed (< 12.8 sec) was obtained with H-WO_3 NFs and NOGR-loaded H-WO_3 NFs, which showed high potential for application in portable and real-time diagnosis of diabetes by exhaled breath analysis.

Acknowledgement

This work was supported by the Center for Integrated Smart Sensors funded by the Ministry of Science, ICT & Future Planning as Global Frontier Project (CISS-2011-0031870) and the energy efficiency and resources of the Korea Institute of Energy Technology Evaluation and Planning (KETEP) grant funded by the Ministry of Knowledge Economy, Korean government (No: 20122010100140).

Notes and references

[a]*Department of Material Science and Engineering, Korea Advanced Institute of Science and Technology (KAIST), Daejeon 305–701, Republic of Korea. E-mail address: idkim@kaist.ac.kr; Fax: +82-42-350-5329; Tel: +82-42-350-3329*

[b]*Department of Materials Science and Engineering and Graphene Research Center of KI for the NanoCentury, Korea Advanced Institute of Science and Technology, Daejeon 305-701, Republic of Korea.*

†Electronic Supplementary Information (ESI) available: Experimental details, TEM nalysis of dense and porous WO_3 NFs, EDS elemental mapping analysis, XRD analysis, SEM and TEM analysis of as-spun W precursor/PVP/PS composite NFs, limit of detection characteristic, and UPS analysis. See DOI: 10.1039/b000000x/

1. G. Peng, U. Tisch, O. Adams, M. Hakim, N. Shehada, Y. Y. Broza, S. Billan, R. Abdah-Bortnyak, A. Kuten and H. Haick, *Nat. Nanotechnol.*, 2009, **4**, 669-673.
2. E. Tseliou, V. Bessa, G. Hillas, V. Delimpoura, G. Papadaki, C. Roussos, S. Papiris, P. Bakakos and S. Loukides, *Chest*, 2010, **138**, 107-113.
3. A. Tangerman and E. G. Winkel, *J. Breath Res.*, 2010, **4**, 017003.
4. M. Righettoni, A. Tricoli and S. E. Pratsinis, *Anal. Chem.*, 2010, **82**, 3581-3587.
5. S. J. Choi, I. Lee, B. H. Jang, D. Y. Youn, W. H. Ryu, C. O. Park and I. D. Kim, *Anal. Chem.*, 2013, **85**, 1792-1796.
6. G. Peng, E. Trock and H. Haick, *Nano Lett.*, 2008, **8**, 3631-3635.
7. S. J. Pearton, F. Ren, Y. L. Wang, B. H. Chu, K. H. Chen, C. Y. Chang, W. Lim, J. S. Lin and D. P. Norton, *Prog. Mater. Sci.*, 2010, **55**, 1-59.
8. I. D. Kim, A. Rothschild and H. L. Tuller, *Acta Mater.*, 2013, **61**, 974-1000.
9. J. Shin, S. J. Choi, I. Lee, D. Y. Youn, C. O. Park, J. H. Lee, H. L. Tuller and I. D. Kim, *Adv. Funct. Mater.*, 2013, **23**, 2357-2367.
10. C. W. Na, H. S. Woo, I. D. Kim and J. H. Lee, *Chem. Commun.*, 2011, **47**, 5148-5150.
11. H. G. Moon, Y. R. Choi, Y. S. Shim, K. I. Choi, J. H. Lee, J. S. Kim, S. J. Yoon, H. H. Park, C. Y. Kang and H. W. Jang, *ACS Appl. Mater. & Interfaces*, 2013, **5**, 10591-10596.
12. M. Behl, J. Yeom, Q. Lineberry, P. K. Jain and M. A. Shannon, *Nat. Nanotechnol.*, 2012, **7**, 810-815.
13. H. R. Kim, K. I. Choi, K. M. Kim, I. D. Kim, G. Z. Cao and J. H. Lee, *Chem. Commun.*, 2010, **46**, 5061-5063.
14. Y. E. Chang, D. Y. Youn, G. Ankonina, D. J. Yang, H. G. Kim, A. Rothschild and I. D. Kim, *Chem. Commun.*, 2009, 4019-4021.
15. S. J. Choi, M. P. Kim, S. J. Lee, B. J. Kim and I. D. Kim, *Nanoscale*, 2014, **6**, 11898-11903.
16. X. L. Li, T. J. Lou, X. M. Sun and Y. D. Li, *Inorg. Chem.*, 2004, **43**, 5442-5449.
17. J. H. Lee, *Sens. Actuators*, 2009, **140**, 319-336.
18. C. Wang, X. Cheng, X. Zhou, P. Sun, X. Hu, K. Shimanoe, G. Lu and N. Yamazoe, *ACS Appl. Mater. & Interfaces*, 2014, **6**, 12031-12037.
19. M. R. Alenezi, S. J. Henley, N. G. Emerson and S. R. P. Silva, *Nanoscale*, 2014, **6**, 235-247.
20. D. P. Volanti, A. A. Felix, M. O. Orlandi, G. Whitfield, D. J. Yang, E. Longo, H. L. Tuller and J. A. Varela, *Adv. Funct. Mater.*, 2013, **23**, 1759-1766.
21. X. C. Jiang, T. Herricks and Y. N. Xia, *Nano Lett.*, 2002, **2**, 1333-1338.
22. T. Ghoshal, S. Biswas, S. Kar, A. Dev, S. Chakrabarti and S. Chaudhuri, *Nanotechnology*, 2008, **19**, 065606.
23. H. Y. Dang, J. Wang and S. S. Fan, *Nanotechnology*, 2003, **14**, 738-741.
24. D. J. Yang, I. Kamienchick, D. Y. Youn, A. Rothschild and I. D. Kim, *Adv. Funct. Mater.*, 2010, **20**, 4258-4264.
25. S. J. Choi, B. H. Jang, S. J. Lee, B. K. Min, A. Rothschild and I. D. Kim, *ACS Appl.Mmater. & Interfaces*, 2014, **6**, 2587-2596.
26. S. J. Choi, F. Fuchs, R. Demadrille, B. Grevin, B. H. Jang, S. J. Lee, J. H. Lee, H. L. Tuller and I. D. Kim, *ACS Appl. Mater. & Interfaces*, 2014, **6**, 9061-9070.
27. S.-J. Choi, W.-H. Ryu, S. Kim, H.-J. Cho and I.-D. Kim, *J. Mater. Chem. B*, 2014.
28. S. M. Cui, G. H. Lu, S. Mao, K. H. Yu and J. H. Chen, *Chem. Phys. Lett.*, 2010, **485**, 64-68.
29. X. G. Wen, Y. P. Fang, Q. Pang, C. L. Yang, J. N. Wang, W. K. Ge, K. S. Wong and S. H. Yang, *J. Phys. Chem. B*, 2005, **109**, 15303-15308.
30. G. Gu, B. Zheng, W. Q. Han, S. Roth and J. Liu, *Nano Lett.*, 2002, **2**, 849-851.
31. K. H. Park, B. H. Kim, S. H. Song, J. Kwon, B. S. Kong, K. Kang and S. Jeon, *Nano Lett.*, 2012, **12**, 2871-2876.
32. S. H. Song, K. H. Park, B. H. Kim, Y. W. Choi, G. H. Jun, D. J. Lee, B. S. Kong, K. W. Paik and S. Jeon, *Adv. Mater.*, 2013, **25**, 732-737.
33. J. Kwon, S. H. Lee, K. H. Park, D. H. Seo, J. Lee, B. S. Kong, K. Kang and S. Jeon, *Small*, 2011, **7**, 864-868.

34. Y. Hernandez, V. Nicolosi, M. Lotya, F. M. Blighe, Z. Y. Sun, S. De, I. T. McGovern, B. Holland, M. Byrne, Y. K. Gun'ko, J. J. Boland, P. Niraj, G. Duesberg, S. Krishnamurthy, R. Goodhue, J. Hutchison, V. Scardaci, A. C. Ferrari and J. N. Coleman, *Nat. Nanotechnol.*, 2008, **3**, 563-568.
35. R. S. Khadayate, V. Sali and P. P. Patil, *Talanta*, 2007, **72**, 1077-1081.